

Development of optimal multiscale patterns for digital image correlation via local grayscale variation

G.F. Bomarito · J.D. Hochhalter · T.J. Ruggles

Abstract In some applications of digital image correlation (DIC), adequately quantifying deformation of a material can require identification of local deformations which are much smaller than the total field of interest. Instead of exhaustively stitching together images taken at high magnification, it is more efficient to utilize multiple magnifications. Unfortunately, it is rare that the material naturally has features that are useful for image correlation at multiple magnifications. Therefore, an ideal pattern was sought that (1) contains features appropriate for the multiple magnifications, (2) need not know location of high magnification *a priori*, and (3) can be viewed with standard DIC equipment. An optimization framework was developed based on the inclusion of local grayscale biases which can produce multiscale DIC patterns that satisfy these criteria. Numerical and physical experiments were also performed to illustrate the functionality and utility of the designed patterns.

Keywords image correlation · pattern optimization · multiscale

1 Introduction

In many applications of digital image correlation (DIC), it is advantageous to have measurements at multiple

G.F. Bomarito
National Aeronautics and Space Administration, Langley Research Center, Hampton, VA
E-mail: geoffrey.f.bomarito@nasa.gov

J D. Hochhalter
National Aeronautics and Space Administration, Langley Research Center, Hampton, VA

T.J. Ruggles
National Institute of Aerospace, Hampton, VA, USA

scales [1–5] in order to adequately quantify deformation of a material where localized phenomena occur within a larger field of interest. Although increased magnification enables the measurement of local deformation, the resulting images have a field of view much smaller than the total field of interest. While such images could be stitched together to cover the total field of interest, this would require a complex experimental setup and a higher computational burden, in addition to any errors introduced by the stitching process. Utilization of multiple scales of DIC measurements is a more efficient solution. It allows for the accurate quantification of localized deformation using high magnification and is able to put them in the context of the entire field of view using low magnification.

Occasionally, the specimen of interest is well suited for multiscale DIC, having a well-textured surface as visible from many different magnifications, e.g. organic materials such as wood [3]. However, more frequently it is the case that the natural texture at one or all of the length scales of interest is insufficient for adequate DIC measurements to be made. In these cases, a pattern must be applied to the specimen at the scales of interest. Unfortunately, most commonly used patterning methods are not well suited for use at multiple length scales. The problem lies in the fact that optimal magnification is linked to the average speckle size of the pattern [6–12] and that most patterning methods offer a limited range of speckle sizes [9–12].

The issue can be approached in multiple ways. Firstly, it can be completely circumvented via domain division [4], where different patterns are used in different regions of a specimen, but this requires knowledge of the locations of the features of interest at the different scales *a priori*. A second simple solution would be to apply two patterns of varying speckle sizes to the same specimen;

however, traditional methods of pattern application interfere with each other. As an example, consider the use of spray paint and airbrush on the same surface such that many large and small speckles exist. At the smaller scale, entire regions of the pattern would be covered by a single large speckle leaving large areas unusable by DIC. Thirdly, other promising methods such as multi-spectrum DIC [1] aim to combat this cross pattern interference but they are application specific and generally require specialized equipment. Lastly, the approach pursued in the current work, is to design a single pattern that is well suited for DIC measurements at multiple length scales. Furthermore, since Bomarito et al. [13] showed a method in which DIC patterns can be optimized to produce lower DIC measurement error, a pattern that is specifically designed to minimize DIC errors at multiple scales is pursued.

The basis of the method developed herein was illustrated by Bossuyt et al. [14] who showed that multiscale DIC patterns can be developed by altering the frequency content of a pattern's auto-correlation function to include spikes at distinct length scales. The same idea, in the spatial domain of the pattern rather than the frequency domain, is to vary the average grayscale value of a pattern locally, such that the pattern contains contrasting features at multiple length scales. By including local grayscale variation within the optimization framework setup by Bomarito et al. [13], the current work is able to produce patterns which (1) can be utilized at multiple magnifications for DIC, (2) need not know location of high magnification *a priori*, (3) can be viewed with standard DIC equipment, and (4) are optimally suited for multiscale DIC under these constraints.

The remainder of the current work is organized as follows. Section 2 reviews the fundamental information on DIC and pattern optimization that is necessary for the proposed method of multiscale pattern creation. The proposed method is outlined in Section 3. Patterns are presented and analyzed with numerical deformation tests in Section 4, and are utilized in a physical multiscale experiment in Section 5. The outcomes are summarized and discussed in Section 6.

2 Background

The basis of DIC is the matching of features between two images, so that relative deformations occurring between the two images can be inferred [17]. Because the matching of the grayscale values of individual pixels would have non-uniqueness issues, subsets of size $(2M+1)$ pixels by $(2M+1)$ pixels are utilized for tracking of features. As a consequence of using subsets, a criterion must be chosen to evaluate the similarity of

subsets between images. This is commonly referred to as a correlation criterion and several are present in the DIC literature [15–17]. The correlation criterion chosen for the current work is the zero-normalized cross-correlation (ZNCC) coefficient:

$$C = \sum_{i=-M}^M \sum_{j=-M}^M \left[\frac{(f(x_i, y_j) - \bar{f}^{(M)})(g(x'_i, y'_j) - \bar{g}^{(M)})}{\Delta f \Delta g} \right] \quad (1)$$

with

$$\begin{aligned} \bar{f}^{(M)} &= \frac{1}{(2M+1)^2} \sum_{i=-M}^M \sum_{j=-M}^M f(x_i, y_j) \\ \bar{g}^{(M)} &= \frac{1}{(2M+1)^2} \sum_{i=-M}^M \sum_{j=-M}^M g(x'_i, y'_j) \\ \Delta f &= \sqrt{\sum_{i=-M}^M \sum_{j=-M}^M (f(x_i, y_j) - \bar{f}^{(M)})^2} \\ \Delta g &= \sqrt{\sum_{i=-M}^M \sum_{j=-M}^M (g(x'_i, y'_j) - \bar{g}^{(M)})^2} \end{aligned} \quad (2)$$

In this definition $f(x_i, y_j)$ is the grayscale value of a pixel at location (x_i, y_j) in the reference image and $g(x'_i, y'_j)$ is the grayscale value at location (x'_i, y'_j) in the deformed image. $\bar{f}^{(M)}$ and $\bar{g}^{(M)}$ are the subset averaged grayscale values in the reference and deformed images, respectively. Δf and Δg are the standard deviations of the subset grayscale values in the reference and deformed images, respectively. While the values of f and g at pixel locations in an image are discrete and depend on the bit depth of the image, they will be referred to as normalized grayscale values ranging from 0.0 (black) to 1.0 (white) throughout the current work. Mapping functions, ξ , from (x_i, y_j) to (x'_i, y'_j) which are commonly referred to as subset shape functions, account for the displacement and distortion of the subset. It is defined formally as $(x'_i, y'_j) = \xi(x_i, y_j)$. In cases where (x'_i, y'_j) are non-integer values it is also necessary to define an interpolation method to evaluate $g(x'_i, y'_j)$ based on pixel image data. This interpolation function η is defined formally with $g(x'_i, y'_j) = \eta(g)$. DIC Displacements are found at location x, y through the optimization of (x', y') so that correlation is maximized, i.e.:

$$u, v = \hat{x}, \hat{y} - x, y \quad (3)$$

where

$$\hat{x}, \hat{y} = \arg \min_{x', y'} C(x, y, x', y', f, g, M, \xi, \eta) \quad (4)$$

given the other components of the correlation criterion f, g, M, ξ , and η . A large effort in the DIC literature has

been to evaluate these components of correlation criteria to quantify the contribution of each to overall DIC measurement error. Specifically, the subset size M [6, 7, 18, 19], shape function choice ξ [17, 20–23], and interpolation function choice η [17, 24, 25] have been widely studied.

2.1 Pattern quality metrics

In addition to the above components, a critical factor in the accuracy of DIC measurements is the image content itself, *i.e.*, f and g . While this can generally cover a multitude of factors such as lighting and camera noise, attention here is restricted to the image patterns themselves which should be responsible for the majority of the information content of the image. The study of the effect of patterns on DIC measurement error has traditionally been focused on quantifying the suitability of a pattern for use with DIC; hence, many pattern quality metrics have been derived [6, 12, 14, 17–19, 25–29]. These metrics have been invaluable in the assessment of pseudo-randomly generated patterns, such as airbrush and spray paint patterns, and offer practical means of decision between patterning options. An example of a commonly used pattern quality metric is the sum of square of subset intensity gradients (SSSIG), which was developed based on the susceptibility of an image to Gaussian noise [17, 19, 25]. In the current work, the following two dimensional definition of SSSIG (denoted S) is used:

$$S(x, y, f) = \sum_{i=-M}^M \sum_{j=-M}^M |\nabla f(x_i, y_j)|^2 \quad (5)$$

where $|\nabla f(x_i, y_j)| = \sqrt{f_x(x_i, y_j)^2 + f_y(x_i, y_j)^2}$. Note that the definition is an extension of the original one dimensional SSSIG definition to two-dimensions in a manner similar to Pan et al. [27]. Implementation of S throughout the current work uses finite difference estimates of the derivatives such that $f_x(x, y) = f(x + 1, y) - f(x, y)$. Any derivatives involving pixels outside the subset (*i.e.*, $f_x(x_M, y_j)$ and $f_y(x_i, y_M)$) are ignored during the summation; this ensures that S is a function of only the pixels within the subset (and not influenced by the surrounding region).

As more modern means of DIC pattern application such as micro stamping [30, 31], lithography [32, 33], and water transfer printing [34] are becoming easier and more efficient to use, designer DIC patterns are becoming more practical. Designer DIC patterns allow for the precise design and arrangement of pattern features. As shown by Bomarito et al. [13], this allows for the design of a pattern in which expected DIC error is minimized.

The pattern optimization framework presented in reference [13] is modified in the current work to produce multiscale DIC patterns; for more details beyond the fundamentals of that framework (covered in the proceeding paragraphs) the reader is referred to reference [13].

The framework is based on the fact that most pattern quality metrics are ill-suited for individual use in pattern optimization, *i.e.*, their utility degrades when approaching best values. For example, a simple checkerboard pattern achieves the best possible value of SSSIG, but is ill-suited for DIC because of its non-uniqueness problems. Bomarito et al. [13] proposed a multi-metric optimization procedure that is able to circumvent this issue. It is based on the use of a combined quality metric:

$$Q(x, y, f) = \hat{S} + w_1(\hat{A}_2)^{n_1} \quad (6)$$

where the primary term is the normalized SSSIG $\hat{S} = 1 - \frac{S}{8M^2 + 4M}$ and the secondary term, based on \hat{A}_2 , acts as a uniqueness constraint. The constants w_1 and n_1 allow for the adjustment of the importance and severity of the constraint. \hat{A}_2 is a uniqueness measure based on the autocorrelation function; the auto-correlation function A is a correlation of an image with itself, or more precisely: $A(u, v, x, y, f) = C$, where $g = f$ and $x', y' = x + u, y + v$ (C is the correlation criterion defined at the start of Section 2). \hat{A}_2 is defined as the height of the largest secondary autocorrelation peak:

$$\hat{A}_2(x, y, f) = \max_{u, v \notin W} A(u, v, x, y, f) \quad (7)$$

where W is the watershed of the primary autocorrelation peak located at $u, v = 0, 0$. Hence, a value of $\hat{A}_2 = 1$ corresponds to a perfect match of a subset with another nearby subset. It is assumed in the current work that two regions separated by more than $2M$ are independent of each other; thus, the auto-correlation range $-(2M + 1) \leq u, v \leq 2M + 1$ is used.

2.2 Pattern optimization

As a step in the pattern optimization process, the pattern must be parameterized. This parameterization could be chosen in many different ways, for example as the number, size, and locations of circular speckles. In the current work, as in Bomarito et al. [13], the target application is one where the resolution of the patterning method is higher than the desired magnification of the smallest scale of interest. For this reason a bitmap image wherein each pixel is represented by a Boolean parameter is chosen for the parameterization of the pattern. Note that the proceeding objective function and

optimization methodology are independent of this parameterization.

Relying on the relative independence of spatially separated regions, Bomarito et al. [13] broke down the optimization of a pattern into many sequential sub-optimizations of individual (non-overlapping) sub-regions of the pattern. The goal of each of the sub-optimizations was the minimization of the mean Q value of all the subsets centered at pixels within that sub-region, *i.e.*,

$$f_{opt}(x, y) = \arg \min_{f(x, y)} \bar{Q}^{(N)}(x, y, f) \quad (8)$$

with

$$\bar{Q}^{(N)}(x, y, f) = \frac{1}{N^2} \sum_i^N \sum_j^N Q(x_i, y_j, f) \quad (9)$$

where N is the size of the sub-region and $Q(x_i, y_j)$ is the value of Q of the subset centered at (x_i, y_j) within the sub-region. Sub-regions near the boundary of the pattern are padded assuming a periodic placement of the pattern.

3 Methods

The task of extending the work of Bomarito et al. [13] to multiscale patterns via local grayscale variation is relatively straight forward. A modification of the objective function is introduced at the sub-region level of the optimization procedure. Namely, Equation 8 is modified to include a term for the average grayscale value of the sub-region:

$$f_{opt}(x, y) = \arg \min_{f(x, y)} \bar{Q}^{(N)}(x, y, f) + Q_f(x, y, f) \quad (10)$$

with

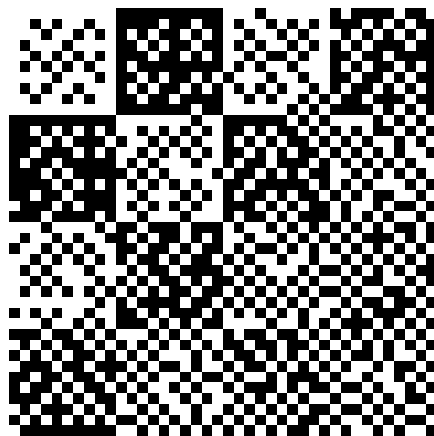
$$Q_f(x, y, f) = \left(\frac{f^* - \bar{f}^{(N)}}{w_2} \right)^{n_2} \quad (11)$$

$$\bar{f}^{(N)} = \frac{1}{N^2} \sum_i^N \sum_j^N f(x_i, y_j)$$

where f^* is the target average grayscale for the sub-region. Essentially, the optimization problem seeks minimization of \hat{S} , while imposing constraints on both uniqueness and local average grayscale value. The parameters w_2 and n_2 , which act in a similar manner to w_1 and n_1 , are used to adjust the range and intensity of the grayscale constraint. For instance, the values $n_2 = \infty$ and $w_1 = 0.05$ ensure that the average grayscale value of the sub-region will be within 0.05 of f^* and that Q_f is uniformly 0 within that range. For all optimizations performed herein, the values of $n_2 = 6$ and $w_2 = 0.15$

are used, which less strictly impose the constraint on $\bar{f}^{(N)}$ and allow for deviations from f^* if they are accompanied by sufficient improvements in $\bar{Q}^{(N)}$.

The intended use of the above equations for multiscale pattern generation is that the value of f^* can be spatially varied, thus inducing local grayscale biases. For example, Figure 1(a) is the result of an optimization performed with f^* values for each sub-region shown in the table in Figure 1(b). The optimization parameters used in this and all subsequent optimizations are shown in Table 1 except for f^* which is varied to produce specific patterns. In this same manner, the spatial modulation of f^* according to a macro-scale mask would be able to produce a macro-scale pattern with micro-scale features throughout.



(a)

0.8	0.2	0.7	0.3
0.2	0.7	0.3	0.6
0.7	0.3	0.6	0.4
0.3	0.6	0.4	0.5

(b)

Fig. 1: A 40 pixel by 40 pixel example of a multiscale pattern with local variations in average grayscale value (a) and target f^* values taken from map (b). Note that each element in map (b) was used for blocks of four sub-regions with $N = 5$ resulting in 10 pixel by 10 pixel blocks.

$2M + 1$	N	w_1	n_1	w_2	n_2
5	5	$\frac{2}{9}$	12	0.15	6

Table 1: Values of parameters used in all optimizations.

Figure 1 illustrates that, within the bounds investigated, the magnitude of the variation of f^* between neighboring sub-regions of the pattern correlates to the degree of contrast between larger-scale features. The top left of the pattern has the highest large-scale contrast, decreasing in the downward and rightward directions. Because of the importance of S (which quantifies pattern contrast) in the determination of pattern quality, large-scale DIC accuracy is expected to be directly related to this large-scale contrast. However, higher large-scale contrast requires more biased grayscale values (f^* deviating further from 0.5) at the smaller-scale.

Table 2 contains a summary of a test which investigated the effect of grayscale bias at the small-scale. In this test, thirteen 100 pixel by 100 pixel patterns were generated using various, spatially-uniform values of f^* . The pattern-averaged grayscale values (\bar{f}), the patterned-averaged Q (denoted \bar{Q}), and the pattern-averaged SSSIG (\bar{S}) are shown along with a 10 pixel by 30 pixel section of each pattern in Table 2. Values were calculated using the parameters listed in Table 1. From the table, it can be seen that the best pattern quality (minimum \bar{Q}) is achieved with an \bar{f} value of approximately 0.5. Furthermore, imposition of a grayscale bias causes the pattern quality to degrade. This is in agreement with Mazzoleni et al. [35], who found that the optimal cover factor is 40%-70%. These results indicate that the use of more biased small-scale patterns has the dual effect of decreasing small-scale quality and increasing larger-scale contrast. Therefore, the generation of multiscale patterns by modulation of local grayscale bias must balance these two effects based on the end use of the pattern.

4 Numerical experiments

Two sets of numerical experiments were performed in order to show the relationship between grayscale bias and expected DIC error at both the large- and small-scale. The numerical experiments generally consisted of the application of numerical deformations to a pattern while simulating other factors such as noise and lighting. The numerical experiments were meant to act as a surrogate to physical DIC experiments, modeling as many factors of realistic conditions as possible. Numerical experiments were chosen because they have a useful














f^*	\bar{f}	\bar{Q}	\bar{S}	Pattern (10x30 pixel section)
0.80	0.760	0.522	19.20	
0.75	0.720	0.444	22.40	
0.70	0.648	0.331	28.17	
0.65	0.600	0.292	30.97	
0.60	0.560	0.279	32.72	
0.55	0.522	0.263	33.69	
0.50	0.501	0.264	33.93	
0.45	0.477	0.271	33.65	
0.40	0.440	0.272	32.55	
0.35	0.400	0.298	30.98	
0.30	0.353	0.328	28.26	
0.25	0.280	0.444	22.40	
0.20	0.240	0.522	19.20	

Table 2: The effect of grayscale bias on the pattern-averaged Q and pattern-averaged SSSIG (\bar{S}). Each pattern is also included for reference.

advantage over physical experiments: the true applied displacement field is known and can be directly compared to the DIC computed displacement field, allowing exact computation of displacement error.

The description of the procedure of the numerical experiment involves the following terminology which are distinguished here for clarity. A pattern bitmap is the parameterized pattern which contains a Boolean bitmap corresponding to black or white speckles. A surface model is a model of a specimen's surface on which the pattern has been printed. DIC images are simulated images taken of the surface model. All of these terms define images with varying degrees of pixel resolution. They are described further in the procedure below.

Given a pattern in bitmap form, the procedure of the numerical experiments is as follows:

1. **The desired magnification of the DIC images, ρ_{mag} , is chosen.** ρ_{mag} defines the DIC-image pixels to pattern-bitmap pixels ratio. For example, $\rho_{mag} = 5$ would correspond to a magnification of 5-by-5 DIC image pixels for every pattern bitmap pixel. This allows for separate investigation of patterns under simulated high or low magnification.
2. **The desired resolution of the surface model, ρ_{mod} , is chosen.** ρ_{mod} defines the surface-model pixels to DIC-image pixels ratio. For all tests $\rho_{mod} = 10$ is used, meaning 10-by-10 surface model pixels correspond to a single DIC image pixel.
3. **The pattern bitmap is enlarged (scaled up) by ρ_{tot} to produce the surface model**, where $\rho_{tot} = \rho_{mod}\rho_{mag}$. This step is taken as the first step in a super-sampling method for applying deformations. In general, a super-sampling method scales up an image, then deforms it, and finally coarsens the image back to the desired size. Multiple types of numerical deformations have been used in the literature such as FFT shifts [10, 11, 23, 24, 26, 27], polynomial interpolation [9, 26, 36], and super-sampling [35] including some comparative studies [37, 38]. The super-sampling method is chosen here because its binning method bears resemblance to a charge-coupled device (CCD) sensor and because deformation methods between the scaling operations were observed to have little effect on results.
4. **The contrast of the surface model is reduced**, simulating imperfect lighting conditions: *i.e.*, the grayscale values are changed from 0.0 and 1.0 to 0.25 and 0.75, respectively.
5. **The surface model is blurred using a Gaussian filter with standard deviation $\sigma = 0.1\rho_{tot}$.** This blurring is meant to simulate the imperfect application of the pattern, *i.e.*, the edges will not be perfectly crisp and are blurred with standard deviation of 10% of the pattern speckle size.
6. **49 numerical deformations are applied to the surface model using cubic polynomial interpolation.** Deformations of various order and magnitude are applied in the x -direction where $U_x(x, y) = ax^b$. The following values of a and b are utilized:

$$b = 0 : a = (0, 5, 10, \dots, 100) \times 10^{-2}$$

$$b = 1 : a = (1, 2, 3, \dots, 10, 15, 20, \dots, 50) \times 10^{-3}$$

$$b = 2 : a = (1, 2, 3, 4, 5) \times 10^{-5}$$

$$b = 3 : a = (2, 4, 6, 8, 10) \times 10^{-8}$$

7. **The surface model images are coarsened to produce the DIC images with the desired mag-**

nification. The coarsening is performed by taking the mean of ρ_{mod} pixel by ρ_{mod} pixel bins.

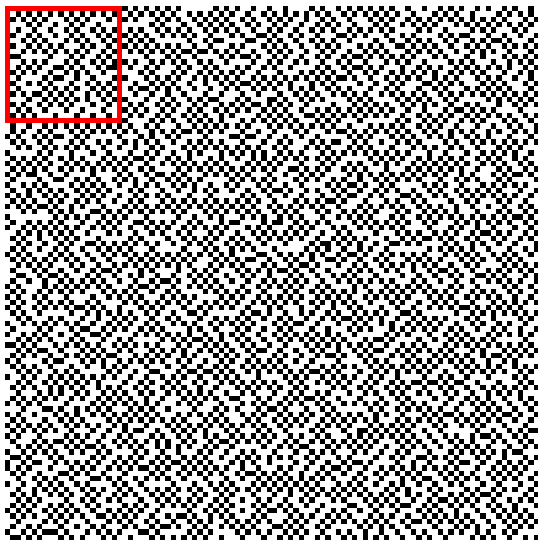
8. **Zero-mean Gaussian white noise with standard deviation $\sigma = 0.02$ is added to the images** to simulate random error in the imaging process. The value of 2% noise is chosen based on the estimation of imaging noise in the work of Zhou et al. [39].
9. **The 49 DIC images are analyzed with DIC.** The image with no deformation ($a = b = 0$) is used as the reference image. The commercial DIC software VIC2D v2009.1.0 by Correlated Solutions [40] is used to analyze the images. The zero-normalized squared difference correlation criterion (equivalent to ZNCC [27]) is utilized. Subset size of 25 pixels, step size of 5 pixels, optimized 4-tap interpolation, and Gaussian subset weights are also used.
10. **The DIC error in the loading direction is calculated:** $\epsilon_x = \tilde{U}_x - U_x$.
11. **Pattern error metrics E_{bias} , E_{std} , and E_{rms} are calculated.** These measures are aggregate measures of the error in the queried points within all 48 deformed images. E_{bias} represents the tendency of the pattern to produce bias measurements and is equal to the mean of all ϵ_x . E_{std} represents the pattern's susceptibility to random error and is equal to the standard deviation of all ϵ_x . Finally, as in references [21, 35], E_{rms} is used as an indicator of total error effectively combining bias and random errors into a single measure. It is defined as the root mean square of all ϵ_x .

In summary, given a pattern bitmap, the procedure above evaluates the DIC error metrics E_{bias} , E_{std} , and E_{rms} , which are based on many numerical deformations of the pattern.

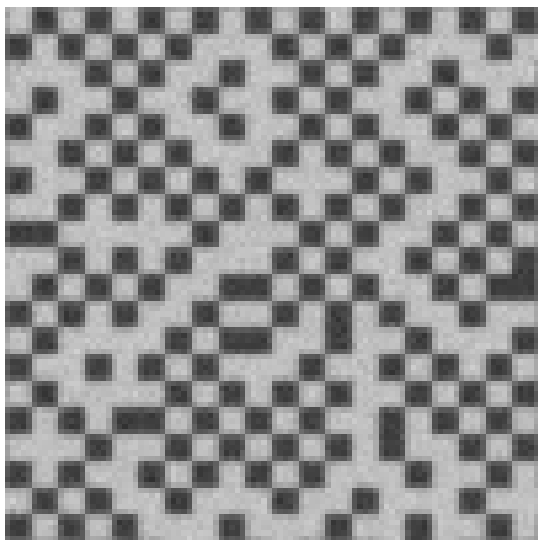
4.1 Small-scale test

The first test investigates the effect of average grayscale bias on DIC error at the small-scale (high magnification), in which all pattern bitmap elements are clearly visible in the images. In this test a relatively high magnification is used of $\rho_{mag} = 5$, meaning 5 by 5 DIC image pixels correspond to each pattern bitmap pixel. An example of a pattern bitmap and one of its generated DIC images is shown in Figure 2.

The 13 patterns from Section 3 (shown in Table 2) which were optimized using various spatially uniform values of f^* are again used in this test. Each of these 100 pixel by 100 pixel patterns were subjected to the procedure outlined above to produce values of E_{bias} , E_{std} , and E_{rms} . The values of all these error metrics are plot-



(a)



(b)

Fig. 2: A section of the 100 pixel by 100 pixel optimized pattern bitmap with $f^* = 0.65$ (a) and a section of its numerically generated DIC reference image with $\rho_{mag} = 5$ (b). The red box in (a) illustrates the portion of pattern bitmap that is seen in (b).

ted with respect to the target grayscale values of their patterns in Figure 3. In this figure it can be seen that bias errors (E_{bias}) are 3 to 4 times smaller than random errors (E_{std}). Furthermore, it seems that no clear trend exists between grayscale bias and error bias, and that E_{bias} remains relatively constant despite changes in f^* . However, there is a clear bowl-type trend between E_{std}

and f^* indicating that the lowest random error is expected in the region near $f^* = 0.5$, with increasing values of random errors as f^* deviates from 0.5. Because E_{std} is much greater than E_{bias} in this test, E_{rms} is dominated by the random errors and shows essentially the same bowl-type curve. Qualitatively, these trends are consistent with what might be expected based on the \bar{S} values of the patterns detailed in Table 2.

4.2 Large-scale test

The second test investigates the effect of average grayscale bias on DIC error at the large-scale (low magnification), in which multiple pattern bitmap features are coarsened into a single image pixel. For this test $\rho_{mag} = 0.2$ meaning 5 by 5 pattern bitmap pixels correspond to a single DIC image pixel. The variation of the average grayscale bias is what creates contrasting regions at the large-scale. This is illustrated in Figure 4 which shows an example of a pattern bitmap and its generated DIC image for the current test.

Five patterns are created for the large-scale test in the following manner. First, two contrasting pattern templates are chosen from the previously generated 100 by 100 pixel pattern bitmaps. The template patterns were chosen to give varying levels of contrast with respect to each other; the five sets of light and dark f^* pairs are (0.8, 0.2); (0.75, 0.25); (0.7, 0.3); (0.65, 0.35); and (0.6, 0.4). Next, the template patterns are tiled 25

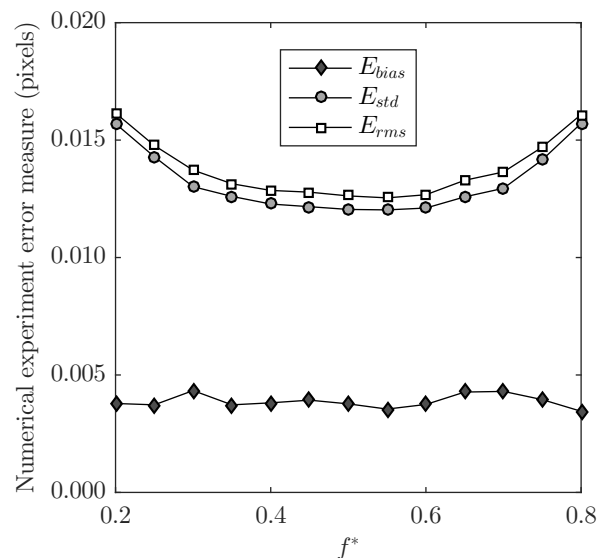
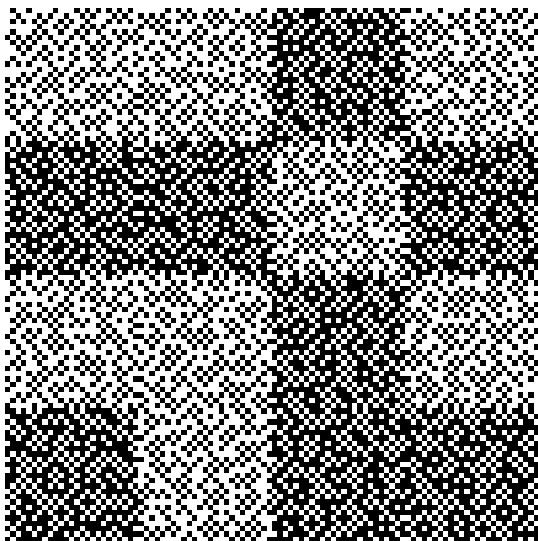
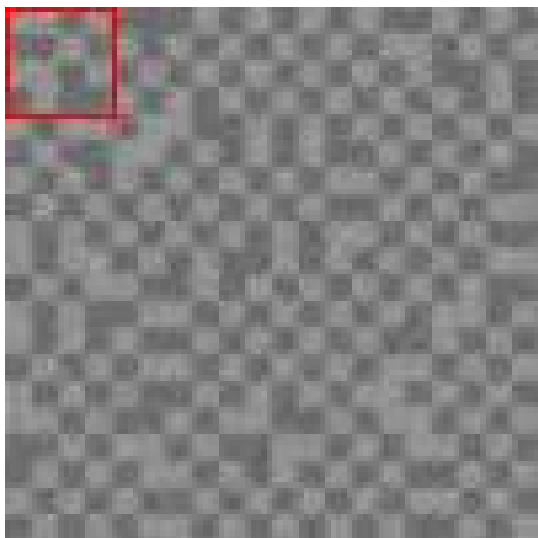


Fig. 3: Results of small-scale numerical experiment. Error metrics from a suite of numerical deformation tests are shown with respect to variations in average grayscale bias.



(a)



(b)

Fig. 4: A section of a multiscale optimized pattern bitmap with local grayscale bias varying between $f^* = 0.3$ and $f^* = 0.7$ (a) and its numerically generated DIC reference image with $\rho_{mag} = 0.2$ (b). The red box in (b) illustrates the portion of the DIC image that corresponds to (a).

times (25 is the chosen ratio of large- to small-scale) resulting in two 2,500 by 2,500 pixel template patterns. Finally, the $f^* = 0.5$ pattern is used as a large-scale mask by which blocks of 25 by 25 pixels from the dark and light templates are chosen (see Figure 4(a)). This same large-scale mask is used for all 5 patterns so that the results of this test rely solely on the contrast between template patterns.

It should be noted that the patterns for this test could have been constructed through an optimization using the $f^* = 0.5$ pattern as a template for local variation in f^* ; however, the above template-based method is chosen for convenience. The main difference is that the borders between neighboring dark and light regions have not been explicitly optimized in the template-based method. In the objective function for any given sub-region / sub-optimization only the \hat{A}_2 term depends on neighboring regions. This term, which is based on the most highly correlated neighboring region, is not likely to be controlled by neighboring regions with greatly different f^* values. Thus, in cases where the ratio between large- and small-scale is high (corresponding to low density of border regions) or largely differing templates are chosen, the use of a template-based method is justified.

Figure 5 shows the results of subjecting the 5 patterns to the suite of numerical deformation tests above. Similar to the small-scale tests, E_{bias} is relatively low in all cases. Because E_{bias} is small relative to E_{std} , E_{rms} nearly coincides with E_{std} . E_{std} shows a clear trend with the changes in template patterns. The templates with similar values of f^* (lower contrast) correspond to higher errors. Ergo, with respect to large-scale DIC, the templates with larger variation in f^* are preferable because they consist of more highly contrasting large-scale features.

4.3 Choice of pattern

In the above two experiments it was shown that grayscale bias away from $f^* = 0.5$ has the dual effect of increasing DIC error at the small-scale and decreasing DIC error at the large-scale. Thus, any choice of the grayscale bias in a multiscale pattern must take both of these effects into consideration. A simple means of doing this is to plot the data from Figures 3 and 5 simultaneously (see Figure 6) so that a simple cost-benefit analysis can be performed. Figure 6 illustrates the expected level of precision at both the large- and small-scales given the choice of grayscale bias for the constituent parts of the pattern. Since these estimated values are derived under consistent conditions the relative accuracy of the two

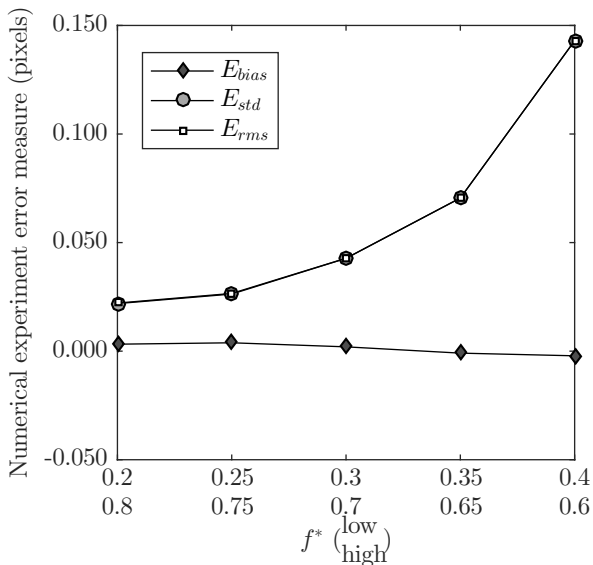


Fig. 5: Results of large-scale numerical experiments. Error metrics from a suite of numerical deformation tests are shown with respect to variations in dark and light template patterns.

scales is assumed to be consistent despite any inaccuracies of the numerical model compared to reality. Furthermore, it should be noted that adjustment of DIC parameters at one scale (*e.g.*, subset size [18, 19, 12] and pre-filtering methods [35, 41, 39]) can effectively reduce the error at that scale while leaving the other scale unaffected.

The application drives the choice of pattern. For instance, if high levels of precision are required at the small-scale and less is needed at the large-scale, grayscale biases of $f^* = 0.4, 0.6$ may provide the best results. Because no single pattern is best suited for all applications, a script for the creation of multiscale patterns in the manner described above is included in the supplementary material of the current work to allow pattern creation suitable for a variety of applications. In the next section, the multiscale pattern with values of $f^* = 0.3, 0.7$ is chosen because it offers a good balance of precision at both scales.

5 Physical experiment

A physical experiment was performed to illustrate the utility and functionality of the generated multiscale patterns. In the experiment, the previously designed pattern with local grayscale bias varying between $f^* = 0.3$ and $f^* = 0.7$ is used (shown in Figure 4(a)). The pattern was applied to an aluminum plate via the water transfer method [34]. Two stereo DIC systems with dif-

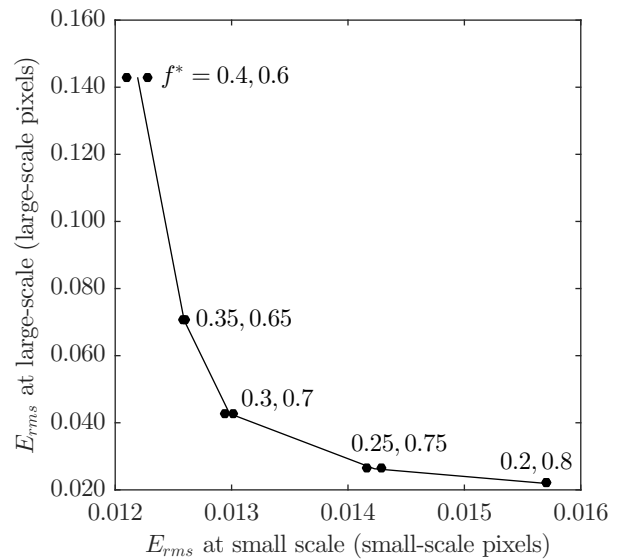
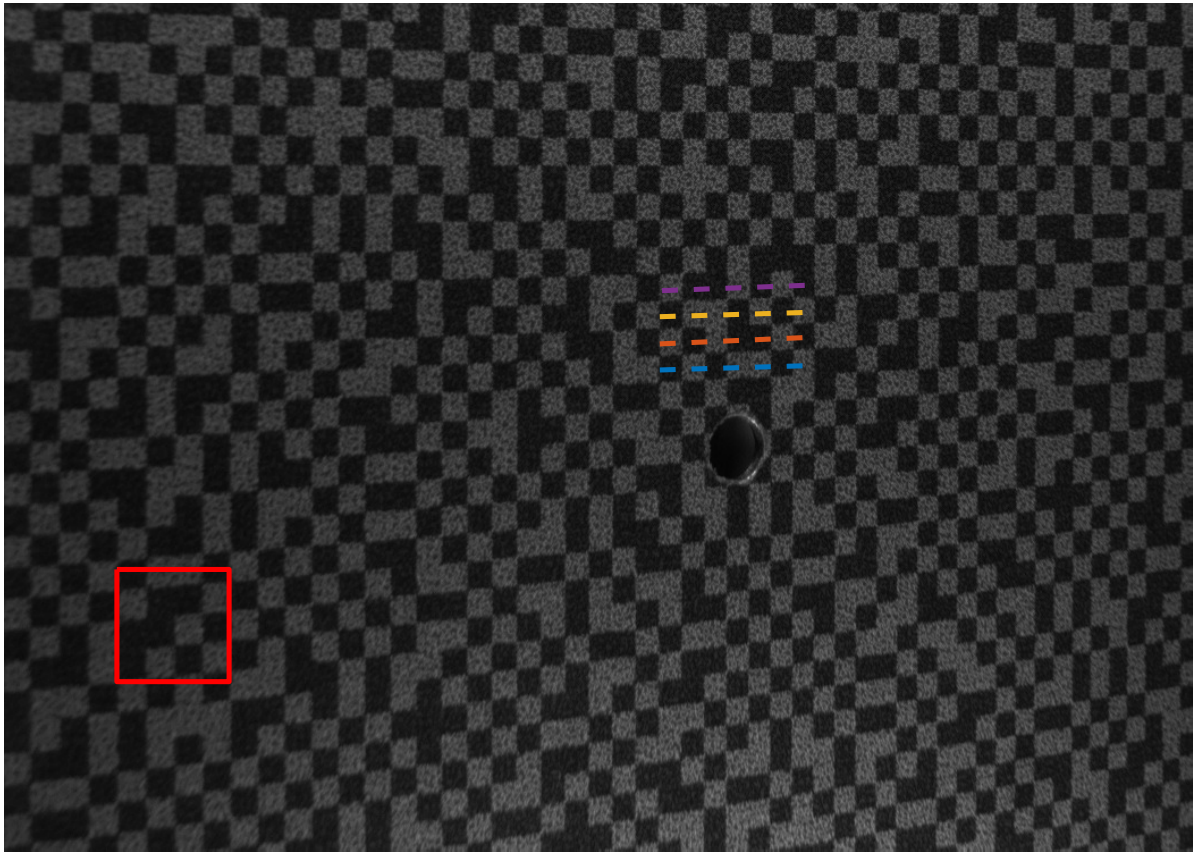


Fig. 6: Tradeoff between large-scale DIC precision and small-scale DIC precision based on choice of local values of f^*

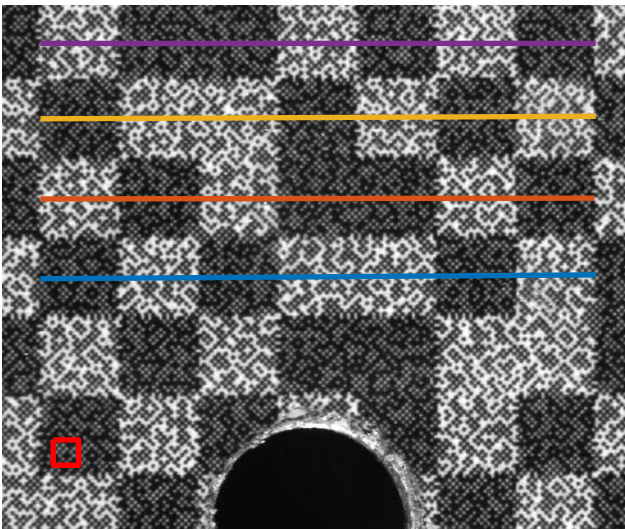
fering levels of magnification were used to image the specimen. The difference in magnification between the two was roughly 16x. Both systems were appropriately calibrated using standard calibration procedures [40]. To illustrate that the pattern performs well at both scales regardless of location, a hole was drilled in the specimen in an arbitrarily located position. The location of both imaging systems was set to include the region near the hole. Figures 7(a) and (b) show examples of the images taken with each DIC system.

The specimen was then loaded in uniaxial tension in a direction just off the vertical y -axis in Figures 7(a) and (b). A higher amount of localized deformation is expected near the hole in the vertical direction. Images were taken before and during loading and DIC was performed to measure displacements. The DIC parameters utilized in step 9 of the numerical experiments in Section 4 are again used here with the exception of subset size. For consistency in the DIC algorithm, a subset size of 99 was used in analysis of both magnification levels; this subset size is shown relative to the patterns as red boxes in Figures 7(a) and (b).

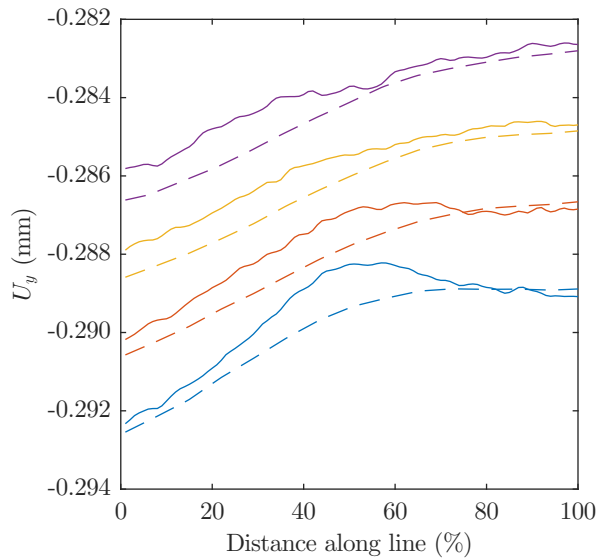
In Figure 7(c), the measured DIC displacements are compared for the two magnifications along the 4 cross-sectional lines which are illustrated in Figures 7(a) and (b). It is seen that the high magnification DIC measurements are able to resolve the localized deformation around the hole much better than with low magnification. The low magnification tends to smear the deformation over a larger area. Especially in cases where strains (spatial derivatives of the displacements mea-



(a)



(b)



(c)

Fig. 7: Physical experiment showing (a) one of the Reference DIC images taken at low magnification, (b) one of the reference images taken at high magnification, and (c) cross-sections of the DIC displacement fields under load. The colored lines in (a) and (b) indicate the locations of the correspondingly colored cross-sections in (c). Dotted lines are used for the low magnification and solid lines are used for the high magnification. The red squares in (a) and (b) illustrate the subset size used in the DIC analysis.

surements) are important, the high magnification using the small pattern features is preferred. In these cases the large-scale strains may not even capture local strain features at all. Figure 7 also shows that as the distance between measurement location and the hole increases, the measurements at the two scales become more similar to each other. This illustrates that both scales can measure the same displacement in a relatively uniform displacement field. Further, by overlaying the displacement fields of the high magnification on the low magnification fields in Figure 8, good agreement is seen at the border of the regions.

As a demonstration of the utility of the pattern in practical multiscale DIC, the strains fields of the two regions are shown in 9. The smoothed strain fields were calculated with 13 by 13 Gaussian weighting. Under high magnification the strain concentration associated with the hole can also be seen. Qualitatively, the magnitude of the strains at the border between the high and low magnifications match relatively well when discounting some edge-effects due to the smoothing process on the high magnification field.

6 Discussion

It has been shown in the current work that multiscale patterns can be created through a modification of the framework of Bomarito et al.[13] by the introduction of a constraint on local average grayscale. This constraint was shown to locally push the pattern away from the optimal DIC pattern as the grayscale bias deviated from $f^* = 0.5$. However, this local bias allows for the resolution of contrasting regions at lower magnifications. Thus, local grayscale biasing has the dual effect of increasing DIC error at high magnification and decreasing DIC error at low magnification. A simple way of viewing this outcome is by noting that the intensity variation of the pattern must encode all pattern information, and since the same intensity variation is used for both scales, they must share that information content. Nonetheless, an appropriate pattern can be designed by weighing the advantages of higher precision at each of the scales of interest in the specific application of choice. A script which generates a multiscale pattern of the type discussed in Section 4.2 is included in the supplementary material of this article, so that patterns may be specifically tailored to an application of interest.

A physical experiment was performed using a precisely designed multiscale pattern which showed that it (1) could be utilized at multiple magnifications for DIC, (2) did not need to know location of high magnification *a priori*, (3) could be imaged with standard DIC equip-

ment, and (4) was optimally suited for multiscale DIC given these constraints.

Acknowledgements This work was supported by the National Aeronautics and Space Administration's Aeronautics Research Mission Directorate through the Digital Twin effort within the Convergent Aeronautics Solutions project.

References

1. T. Berfield, J. Patel, R. Shimmin, P. Braun, J. Lambros, N. Sottos, *Experimental Mechanics* **47**(1), 51 (2007)
2. J. Carroll, C. Efstathiou, J. Lambros, H. Şehitoğlu, B. Hauber, S. Spottswood, R. Chona, *Engineering Fracture Mechanics* **76**(15), 2384 (2009)
3. S. Haldar, N. Gheewala, K. Grande-Allen, M. Sutton, H. Bruck, *Experimental mechanics* **51**(4), 575 (2011)
4. S. Cornell, W. Leser, J. Hochhalter, J. Newman, D. Hartl, pp. V002T02A010–V002T02A010 (2014)
5. M.C. Casperson, J.D. Carroll, J. Lambros, H. Şehitoğlu, R.H. Dodds, *International Journal of Fatigue* **61**, 10 (2014)
6. C. Lane, R.L. Burguete, A. Shterenlikht, *Proceedings of the XIth International Congress and Exposition* pp. 1–9 (2008)
7. J.C. Dupré, M. Bornert, L. Robert, B. Wattrisse, **6**, 31006 (2010)
8. B. Winiarski, G.S. Schajer, P.J. Withers, *Experimental Mechanics* **52**(7), 793 (2012)
9. D. Lecompte, A. Smits, S. Bossuyt, H. Sol, J. Vantomme, D. Van Hemelrijck, A. Habraken, *Optics and Lasers in Engineering* **44**(11), 1132 (2006)
10. D. Lecompte, S. Bossuyt, S. Cooreman, H. Sol, J. Vantomme, *Proceedings of the Annual Conference and Exposition on Experimental and Applied Mechanics* **3**, 1643 (2007)
11. T. Hua, H. Xie, S. Wang, Z. Hu, P. Chen, Q. Zhang, *Optics & Laser Technology* **43**(1), 9 (2011)
12. G. Crammond, S.W. Boyd, J.M. Dulieu-Barton, *Optics and Lasers in Engineering* **51**(12), 1368 (2013)
13. G. Bomarito, J. Hochhalter, T. Ruggles, A. Cannon, *Optics and Lasers in Engineering* **91**, 73 (2017)
14. S. Bossuyt, *Imaging Methods for Novel Materials and Challenging Applications* **3**, 239 (2013)
15. B. Pan, K. Qian, H. Xie, A. Asundi, *Measurement Science and Technology* **20**(6), 062001 (2009)
16. B. Pan, *Experimental Mechanics* **51**(7), 1223 (2011)
17. M.A. Sutton, J.J. Orteu, H. Schreier, *Image correlation for shape, motion and deformation measurements: basic concepts, theory and applications* (Springer Science & Business Media, 2009)
18. Y. Sun, J.H. Pang, *Optics and Lasers in Engineering* **45**(9), 967 (2007)
19. B. Pan, H. Xie, Z. Wang, K. Qian, Z. Wang, *Optics Express* **16**(10), 7037 (2008)
20. H.W. Schreier, M.A. Sutton, *Experimental Mechanics* **42**(3), 303 (2002)
21. M. Bornert, F. Brémand, P. Doumalin, J.C. Dupré, M. Fazzini, M. Grédiac, F. Hild, S. Mistou, J. Molimard, J.J. Orteu, et al., *Experimental mechanics* **49**(3), 353 (2009)
22. H. Lu, P.D. Cary, *Experimental Mechanics* **40**(4), 393 (2000)

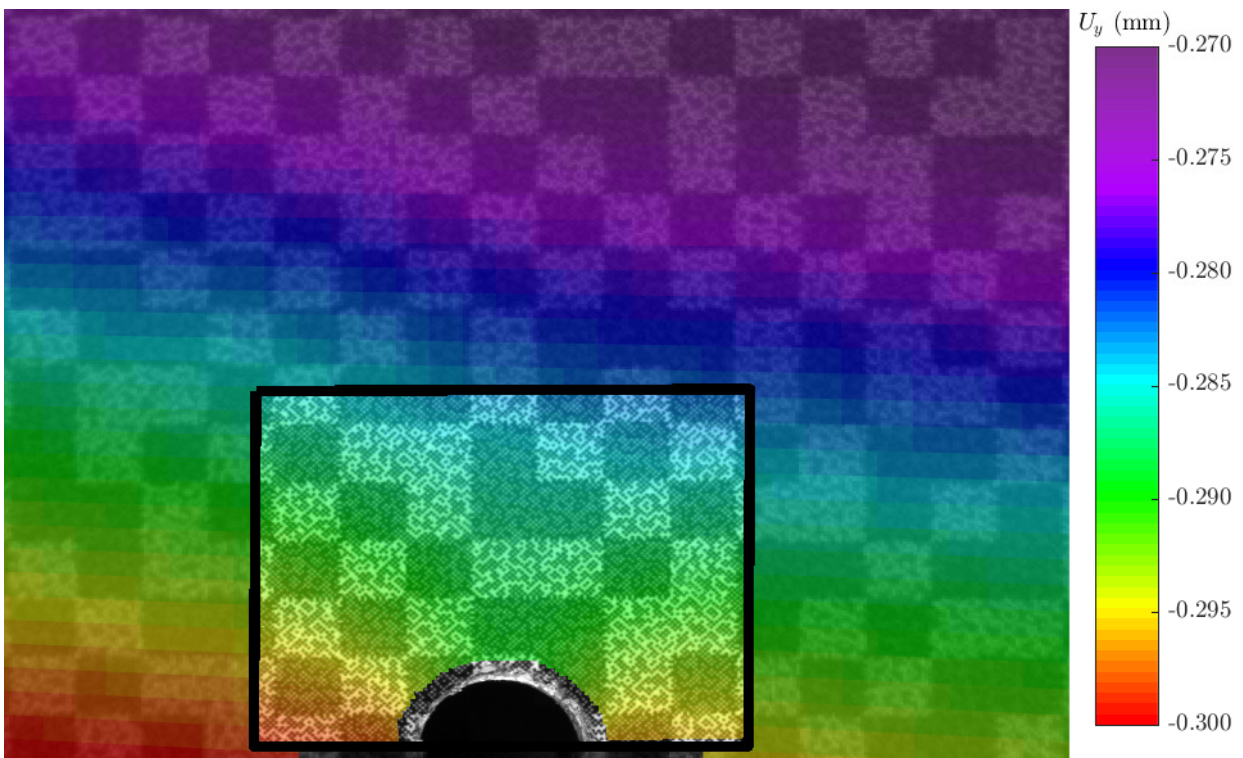


Fig. 8: Overlay of the displacement fields calculated with high and low magnifications. Displacements in the vertical y -direction are shown in millimeters.

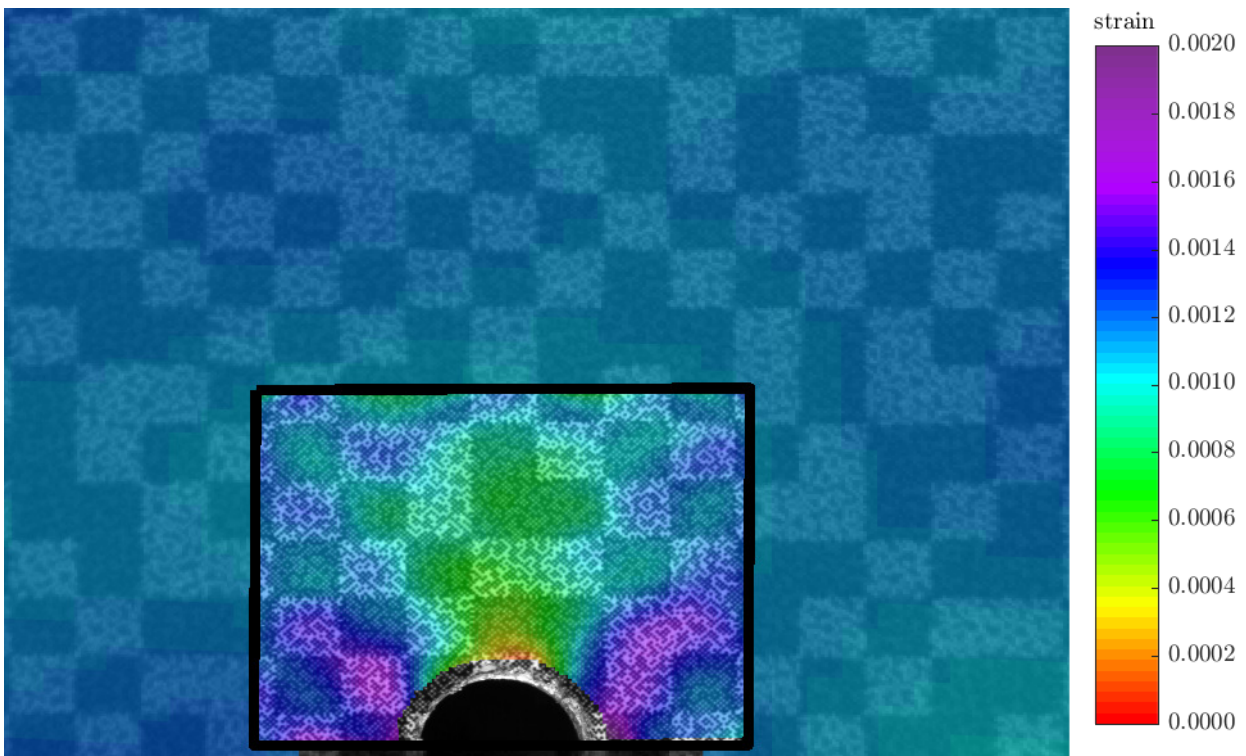


Fig. 9: Overlay of the strain fields calculated with high and low magnifications. The yy component of strain is shown where y is the vertical direction.

23. L. Yu, B. Pan, *Measurement Science and Technology* **26**(4), 045202 (2015)
24. H.W. Schreier, J.R. Braasch, M.A. Sutton, *Optical Engineering* **39**(11), 2915 (2000)
25. Y.Q. Wang, M.A. Sutton, H.A. Bruck, H.W. Schreier, *Strain* **45**(2), 160 (2009)
26. K. Triconnet, K. Derrien, F. Hild, D. Baptiste, *Optics and Lasers in Engineering* **47**(6), 728 (2009)
27. B. Pan, Z. Lu, H. Xie, *Optics and Lasers in Engineering* **48**(4), 469 (2010)
28. J. Park, S. Yoon, T.H. Kwon, K. Park, *Optics and Lasers in Engineering* **91**, 62 (2017)
29. G. Stoilov, V. Kavardzhikov, D. Pashkouleva, *Journal of Theoretical and Applied Mechanics* **42**(2), 55 (2012)
30. A.H. Cannon, J.D. Hochhalter, A.W. Mello, G.F. Bomarito, M.D. Sangid, *Microscopy and Microanalysis* **21**(S3), 451 (2015)
31. T.J. Ruggles, G.F. Bomarito, A.H. Cannon, J.D. Hochhalter, *Microscopy and Microanalysis* (submitted)
32. J.L.W. Carter, M.D. Uchic, M.J. Mills, *Fracture, Fatigue, Failure, and Damage Evolution, Volume 5: Proceedings of the 2014 Annual Conference on Experimental and Applied Mechanics* (Springer International Publishing, Cham, 2015), chap. Impact of Speckle Pattern Parameters on DIC Strain Resolution Calculated from In-situ SEM Experiments, pp. 119–126
33. V.K. Gupta, S.A. Willard, J.D. Hochhalter, S.W. Smith, *Materials Performance and Characterization* **4**(2), 228 (2014)
34. Z. Chen, C. Quan, F. Zhu, X. He, *Measurement Science and Technology* **26**(9), 095201 (2015)
35. P. Mazzoleni, F. Matta, E. Zappa, M.A. Sutton, A. Cigada, *Optics and Lasers in Engineering* **66**, 19 (2015)
36. J.B. Estrada, C. Franck, *Journal of applied mechanics* **82**(9), 095001 (2015)
37. M. Bornert, P. Doumalin, J.C. Dupré, C. Poilâne, L. Robert, E. Toussaint, B. Wattrisse, 15th International Conference on Experimental Mechanics **ICEM15**, 22 (2012)
38. M. Bornert, P. Doumalin, J.C. Dupré, C. Poilane, L. Robert, E. Toussaint, B. Wattrisse, *Optics and Lasers in Engineering* **91**, 124 (2017)
39. Y. Zhou, C. Sun, Y. Song, J. Chen, *Optics and Lasers in Engineering* **65**, 46 (2015)
40. C. Solutions, *Reference Manual* (2009). URL <http://www.correlatedsolutions.com>
41. B. Pan, *Optics and Lasers in Engineering* **51**(10), 1161 (2013)